A MEMS Singlet Oxygen Generator—Part II: Experimental Exploration of the Performance Space

Tyrone F. Hill, Luis Fernando Velásquez-García, Benjamin A. Wilhite, W. Terry Rawlins, Seonkyung Lee, Steven J. Davis, Klavs F. Jensen, Alan H. Epstein, and Carol Livermore, *Member, IEEE*, *Member, ASME*

***Abstract*—This paper reports the quantitative experimental exploration of the performance space of a microfabricated singlet oxygen generator (μSOG). SOGs are multiphase reactors that mix H_2O_2, KOH, and Cl_2 to produce singlet delta oxygen, or $O_2(a)$. A scaled-down SOG is being developed as the pump source for a microfabricated chemical oxygen-iodine laser system because scaling down a SOG yields improved performance compared to the macroscaled versions. The performance of the μSOG was characterized using $O_2(a)$ yield, chlorine utilization, power in the flow, molar flow rate per unit of reactor volume, and steady-state operation as metrics. The performance of the μSOG is measured through a series of optical diagnostics and mass spectrometry. The test rig, which enables the monitoring of temperatures, pressures, and the molar flow rate of $O_2(a)$, is described in detail. Infrared spectra and mass spectrometry confirm the steady-state operation of the device. Experimental results reveal $O_2(a)$ concentrations in excess of 10^{17} cm^{-3}, $O_2(a)$ yield at the chip outlet approaching 80%, and molar flow rates of $O_2(a)$ per unit of reactor volume exceeding 600×10^{-4} mol/L/s. [2007-0163]**

***Index Terms*—Chemical oxygen iodine laser (COIL), infrared (IR) diagnostics, microfluidics, singlet delta oxygen, singlet oxygen generator (SOG).**

I. Introduction

SINGLET delta oxygen [$O_2(a^1\Delta_g)$ or $O_2(a)$] is a spin-excited molecule that is useful for many different applications. It differs from ground-state [triplet, $O_2(X^3\Sigma^-)$, or $O_2(X)$] oxygen in that the number of valence of electrons in each spin state is balanced, resulting in an energy difference of 22.5 kcal/mol between the two states [1]. Chemical oxygen iodine lasers (COILs) are flowing gas lasers that use $O_2(a)$ to pump $I(^2P_{3/2})$ to the higher $I(^2P_{1/2})$ state, from which it then lases at 1.315 μm. COILs are scalable to high powers, making them an attractive alternative to CO_2, hydrogen fluoride, and deuterium fluoride lasers for applications requiring high power and a wavelength that can be transmitted through conventional glass optics. The wavelength also results in a smaller spot size than that of the 10.6-μm wavelength CO_2 system, leading to better resolution and accuracy at higher powers. Since the gain medium is continually and rapidly pumped through the system, the power is not limited by cooling of the lasing medium as it is in solid-state laser systems such as the Nd:YAG [2]. The COIL system is scalable to an average power output in excess of 1 MW [3]. As discussed in Part I of this paper [4] and in [5], singlet oxygen generators (SOGs) produce $O_2(a)$ through a chemical reaction between gaseous Cl_2 and an aqueous mixture of concentrated H_2O_2 and KOH, also known as basic hydrogen peroxide (BHP).

This paper extends the experimental proof of concept provided in Part I (dimol emission, infrared (IR) spectra, and correlation of chlorine injection with oxygen generation) by systematically exploring the operational space of the microfabricated SOG (μSOG) to address whether the device reaches steady state and whether the chlorine is fully reacted, and to determine the highest yield, concentration, and molar flow rate of $O_2(a)$. It was expected that μSOGs would perform better than their macroscale counterparts because reducing the dimensions of the reactor both increases the reaction efficiency (as surface-to-volume ratio increases) and reduces the $O_2(a)$ losses (as residence time in the auxiliary flow paths decreases). The set of measurements described here is intended to confirm this hypothesis. The experimental characterization is made using spectroscopy of the $O_2(a)$ dimol emission, spectroscopy of the spontaneous emission of the $O_2(a \rightarrow X)$ system, and mass spectrometry of the gaseous byproducts. This experimental characterization of the SOG for a COIL system utilizes a direct approach to measure $O_2(a)$ production. It is typical in the COIL field to benchmark the performance of the full COIL by metrics such as small signal gain of the laser, and then extract the SOG performance from models that incorporate the complex internal reactions of the COIL subsystems. In contrast, this paper employs a direct rigorous experimental benchmarking of the pump reactor for a COIL system as an independent entity.

II. Performance Criteria and Testing Methodology

Beyond simply producing $O_2(a)$, there are several other requirements for the SOG for a COIL system, and several metrics by which SOGs are judged in the COIL community. First, the SOG must ensure that as much of the product O_2 as possible is in the $O_2(a)$ state. This is measured by the yield,

Manuscript received February 13, 2007; revised July 17, 2007. This work was supported in part by the Tactical Technology Office, Defense Advanced Research Projects Agency (DARPA), by the Missile Defense Agency, and by the Air Force Research Laboratory (DARPA Order T171/00, Program Code: 4G10; issued by DARPA's Contracts Management Office under Contract MDA972-04-C-0140). Subject Editor A. Ricco.

T. F. Hill, L. F. Velásquez-García, K. F. Jensen, A. H. Epstein, and C. Livermore are with the Massachusetts Institute of Technology, Cambridge, MA 02139 USA (e-mail: tfhill@mit.edu; lfvelasq@mit.edu; livermor@mit.edu).

B. A. Wilhite is with the Department of Chemical Engineering, University of Connecticut, Storrs, CT 06269 USA (e-mail: bwilhite@engr.uconn.edu).

W. T. Rawlins, S. Lee, and S. J. Davis are with Physical Sciences Inc., Andover, MA 01800 USA (e-mail: rawlins@psicorp.com; lee@psicorp.com).

Color versions of one or more of the figures in this paper are available online at http://ieeexplore.ieee.org.

Digital Object Identifier 10.1109/JMEMS.2007.907880

which is the fraction of O_2 in the singlet delta state at a given point in the system. A positive gain COIL system was first demonstrated by McDermott *et al.* in 1978, with a yield of about 40% [6]. Second, the percentage of Cl_2 converted into O_2 (also called the chlorine utilization) should approach 100%, as any unreacted Cl_2 can deactivate the excited I atoms and impede laser operation. Third, the SOG hardware must be as compact as possible for a given output flow of $O_2(a)$. The authors propose that an appropriate performance metric for compactness is the molar flow rate of $O_2(a)$ per unit of reactor volume; a high value of this metric in this case would indicate that an array of microelectromechanical system (MEMS)-based SOGs could produce a total output of $O_2(a)$ that exceeds that of a comparably sized macroscaled SOG. Fourth, the SOG must operate at a low temperature to minimize the amount of water vapor in the output gas flow; water vapor can also deactivate excited I atoms. Fifth, and as described in Part I, the SOG must effectively separate out the liquid byproducts from the gaseous output flow. Finally, the SOG should operate in the steady state given steady-state inputs (pressures, flow rates, and temperatures).

The values of the SOG performance metrics described above have a complex dependence on the flow rates, pressures, and temperatures at different points in the system because these parameters, in turn, impact residence times, the rate of deactivation of $O_2(a)$ by various mechanisms, and whether the KCl reaction products are at sufficient concentration to crystallize and clog the reactor. Precise control and measurement of the operating conditions are necessary in order to fully characterize the SOG performance over the parameter range of interest. The testing apparatus that enables the measurement and control of these parameters is described in Section III, along with the apparatus for measurement of oxygen populations.

A range of diagnostics is required to measure the resulting SOG performance. The simplest of these diagnostics is flow visualization using a microscope and camera. The flow is visualized in the flow distribution channels, the reaction channels, and the capillary separator.

Although it is relatively straightforward to confirm $O_2(a)$ generation [4], quantitatively measuring the $O_2(a)$ and yield pose significant challenges. Typically, SOG performance is determined in the context of a complete COIL system; heuristics are used to estimate yield from small signal gain and laser output along with various losses and efficiencies in the system [7]. In this paper, a suite of more direct diagnostics is instead employed to obtain both qualitative and quantitative information on the $O_2(a)$ population.

Production of $O_2(a)$ can be confirmed by observing the red glow of the $O_2(a)$ dimol emission, either visually as described in Part I or through spectroscopy. The exact mechanism is unknown but has been postulated as

$$2O_2(a) \longrightarrow O_4^* \longrightarrow O_4 + h\upsilon \longrightarrow 2O_2(X). \qquad (1)$$

This emission produces photons of wavelengths 634 and 703 nm, depending on the vibrational state of the resulting $O_2(X)$ molecules, thus falling into the visible range [8]. However, since the dimol emission rate varies with pressure and other factors, drawing quantitative conclusions from it is difficult [9]. In contrast, the decay of solitary $O_2(a)$ molecules into the triplet state, which produces photons in a molecular band centered at 1268 nm, can be used to determine $O_2(a)$ concentration because there is a one-to-one relationship between the photon emission rate and the number of $O_2(a)$ molecules in the field of view. By normalizing the $O_2(a)$ concentration by the initial Cl_2 concentration, the product of the $O_2(a)$ yield and the chlorine utilization can be determined. One method of determining chlorine utilization is to analyze the gaseous byproducts of the SOG, for example, by mass spectrometry, to determine the total oxygen in the flow. Comparing the total oxygen output to the chlorine input yields the chlorine utilization. Alternatively, the $O_2(a)$ concentration and yield-utilization product just after $O_2(a)$ production can be estimated from the concentration and yield-utilization product at the measurement point and models of the deactivation of $O_2(a)$ en route to the measurement point. This estimated value of the yield-utilization product is a lower bound on the value of the chlorine utilization.

One final aspect of the test methodology for this paper is the use of detailed quantitative models of the SOG to better understand and describe its performance. These include models of the reaction channels, models of the $O_2(a)$ loss mechanisms in the outlet flow paths, and models of the supporting subsystems such as the heat exchangers and the capillary separator. These models are described in detail in Section IV, and their application to the analysis of the results is presented in Section VII.

III. Testing Apparatus

A. Packaging

The completed devices were packaged using a Tefzel chuck and Teflon tubing. The plates have machined ports that allow for the reactants and products to enter and exit the chip. Kalrez o-rings enable leak-free operation of the chip over a range of pressures and easy chip assembly to the testing facility. The package materials were chosen for their chemical resistance to BHP and chlorine. For the connection to the chip's gas outlet port, quartz surfaces were chosen in part to minimize $O_2(a)$ deactivation. The packaging scheme is described in greater detail in Part I [4].

B. Testing Rig

All experiments were performed inside a ventilated cabinet because of the toxic and corrosive nature of chlorine gas and BHP. The BHP is stored in a glass-lined stainless steel pressurized reservoir. The BHP is pressure-fed to the chip by introducing He into the vessel that contains the BHP. The helium pressure (and thus, the BHP flow rate) is regulated by a pressure controller (MKS Instruments, Wilmington, MA). The BHP reservoir and μSOG package are connected using Teflon tubing and Upchurch PEEK connectors. The liquid byproducts coming out of the chip are collected in a second reservoir. Both reservoirs were maintained at temperatures between $-20\ ^\circ$C and $-10\ ^\circ$C to minimize BHP decomposition. Ensuring that the

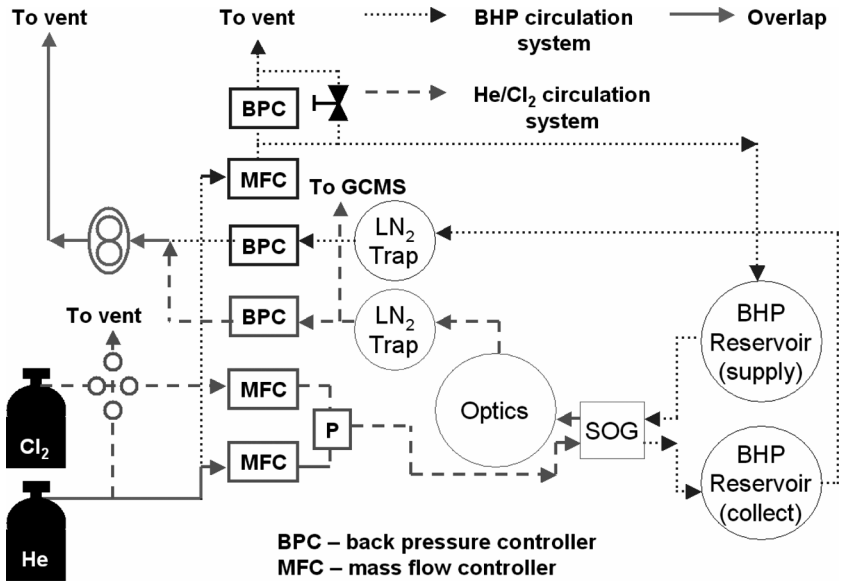

Fig. 1. Schematic of μSOG testing rig.

BHP is properly cooled is critical for safety; at temperatures above 50 °C, H_2O_2 decomposition is accelerated, and the solution can be explosive. Temperatures throughout the testing rig are monitored using thermocouples. Compressed tanks of Cl_2 and He are stored in a cabinet below the experiment, and gas flow to the chip is controlled by mass flow controllers and manual valves. The majority of gas connections preceding the chip use stainless steel tubing and Swagelok connectors. The connections immediately preceding and following the μSOG package are made with Teflon tubing, which was chosen for its flexibility and low reactivity with BHP. Before reaching the vacuum pump, both μSOG exit lines (one for gaseous products and one for liquid byproducts) pass through liquid-nitrogen cooling traps in order to condense water vapor and unreacted chlorine. The gas outlet is then connected to a mass spectrometer through a glass capillary line, allowing sampling of a portion of the plenum stream. The entire setup is served by an external chiller (Julabo, Allentown, PA), which delivers a silicone-based cooling fluid (Syltherm, Dow Chemical, Midland, MI) to the system through Tygon tubing. Fig. 1 illustrates the main features of the testing rig.

C. Oxygen Diagnostics

Singlet delta oxygen concentration measurements were taken using quantitative spectroscopic techniques developed at Physical Sciences Inc., Andover, MA and also described in [10]. The test cell was a rectangular quartz cuvette (Starna, Atascadero, CA) that was connected to the μSOG plenum by a 0.2-cm diameter quartz tube. Collimated optics sampled a cylindrical cross section of the cuvette, yielding a 1.1-cm field of view. The cuvette and collimator are depicted in Fig. 2. In addition to the uncalibrated spectroscopy of the spontaneous $O_2(a)$ decay described in Part I, a liquid-nitrogen-cooled InGaAs array spectrometer (Roper Scientific, Trenton, NJ) was used to analyze photons from the spontaneous emission. The intensity of the spectrometer signal was calibrated to the spectral radiance of a blackbody source at 1000 K. This setup is capable of acquiring a sequence of spectral scans separated by a predetermined integration time. Additionally, a third spectrometer was used to qualitatively measure the intensity of the dimol emission.

Finally, mass spectrometry measurements were made on samples taken from the gas exit line with the intent of using the rise in O_2 mole fraction to determine the degree of chlorine utilization, as described above. To this end, sample gas from the gas outlet flow path was collected by a silica capillary after passing through a liquid-nitrogen trap. The mass spectrometer, which had its intensity calibrated with an 80%/20% He/O_2 mixture, is able to detect constituent elements of the gas stream by first ionizing the molecules and then scanning for certain masses using a quadrupole mass filter.

IV. SOG Design and Model

The $O_2(a)$ production model originates in a series of chemical reactions, which is given in Table I, that describe the interactions between reactants, products, and intermediate compounds. The reaction between Cl_2 and the BHP solution can be described by reactions R1b–R1e. There is significant uncertainty in the rate of the reaction between Cl_2 and BHP [11]–[13]. However, reaction R1b is generally considered to be the rate-limiting step. The mass transfer coefficient can therefore be described by

$$k_L = \sqrt{k_1 \cdot D^l_{\mathrm{Cl}_2} \cdot [\mathrm{O_2H^-}]} \tag{2}$$

where k_1 is the R1b reaction coefficient, $D^l_{\mathrm{Cl}_2}$ is the diffusivity of Cl_2 in BHP, and $[O_2H^-]$ is the peroxide ion concentration. Taking $D^l_{\mathrm{Cl}_2}$ to be 9×10^{-6} cm^2/s [3] and k_1 to be 2.7×10^{10} $\mathrm{cm}^3/\mathrm{mol/s}$ [14], the thickness of the BHP surface layer in which the chlorine reaction occurs is estimated to be about

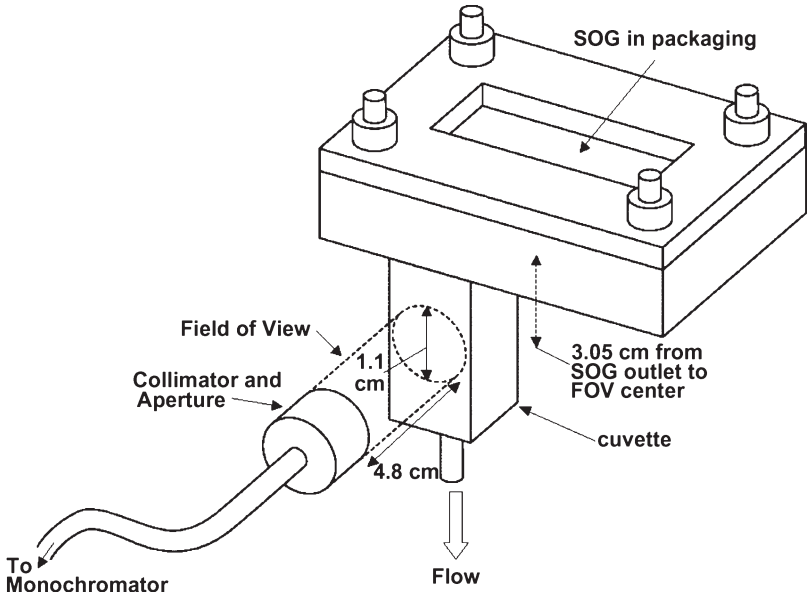

Fig. 2. Schematic of emission measurement setup.

TABLE I
CHEMICAL REACTIONS DESCRIBING THE μSOG DYNAMICS

#	Expression	Rate Coefficient
R1	$H_2O_{2(l)} + 2KOH_{(l)} + Cl_{2(g)} \longrightarrow 2H_2O_{2(l)} + 2KCl_{(l)} + O_2(^1\Delta)_{(g)}$	n.a.
R1a	$OH^- + H_2O_2 \longrightarrow O_2H^- + H_2O$	$K_{eq} > 10^4$
R1b	$O_2H^- + Cl_2 \longrightarrow HOOCl + Cl^-$	$k_1 = 2.7\text{x}10^{10}$ cm^3/mol/s
R1c	$O_2H^- + HOOCl \longrightarrow ClO_2^- + H_2O_2$	K = infinity
R1d	$ClO_2^- \longrightarrow Cl^- + O_2(a)$	K = infinity
R1e	$O_2(a) \longrightarrow O_2(X)$	$K = 5\text{x}10^5$ s^{-1}
R2	$O_2(a) + O_2(a) \longrightarrow O_2(b) + O_2(X)$	$k_2 = 1.63\text{x}10^7$ cm^3/mol/s
R3	$O_2(a) + O_2(a) \longrightarrow O_2(X) + O_2(X)$	$k_3 = 1.02\text{x}10^7$ cm^3/mol/s
R4	$O_2(a) + O_2(X) \longrightarrow O_2(a) + O_2(X)$	$k_4 = 2.35\text{x}10^7$ cm^3/mol/s
R5	$O_2(b) + H_2O \longrightarrow O_2(a) + H_2O$	$k_5 = 4.03\text{x}10^{12}$ cm^3/mol/s
R6	$O_2(b) + Cl_2 \longrightarrow O_2(a) + Cl_2$	$k_6 = 9.03\text{x}10^8$ cm^3/mol/s
R7	$O_2(b) + H_2O_2 \longrightarrow O_2(a) + H_2O_2$	$k_7 = 1.99\text{x}10^{11}$ cm^3/mol/s
R8	$O_2(b) + He \longrightarrow O_2(a) + He$	$k_8 = 6.02\text{x}10^6$ cm^3/mol/s
R9	$O_2(a) + O_2(X) \longrightarrow O_2(X) + O_2(X)$	$k_9 = 9.64\text{x}10^5$ cm^3/mol/s
R10	$O_2(a) + H_2O \longrightarrow O_2(X) + H_2O$	$k_{10} = 2.41\text{x}10^6$ cm^3/mol/s
R11	$O_2(a) + Cl_2 \longrightarrow O_2(X) + Cl_2$	$k_{11} = 3.61\text{x}10^6$ cm^3/mol/s
R12	$O_2(a) + He \longrightarrow O_2(X) + He$	$k_{12} = 4.82\text{x}10^3$ cm^3/mol/s

10 nm. One quantity of interest is the rate of Cl_2 consumption $r_{Cl_2}^-$, which is expressed as

$$r_{Cl_2}^- = k_L \cdot a \cdot [Cl_2]_g \tag{3}$$

where k_L is the mass transfer coefficient, a is the surface area per unit volume, and $[Cl_2]_g$ is the chlorine concentration in the gas. This expression assumes that the reaction at the liquid interface is so rapid that the rate is mass transfer limited, and the interfacial concentration of chlorine is very small. This equation can be further simplified by applying the ideal gas law for the chlorine, which yields

$$r_{Cl_2}^- = k_L \cdot a \cdot y_{Cl_2} \frac{P}{RT} \tag{4}$$

where P is the total pressure, y_{Cl_2} is the chlorine molar fraction, R is the universal gas constant, and T is the temperature of the gas. After the $\mathrm{O}_2(\mathrm{a})$ is produced, it diffuses out of the BHP and into the gas phase. The rate of increase of $\mathrm{O}_2(\mathrm{a})$ in the gas phase is given by

$$r_{\mathrm{O}_2(\mathrm{a})} = k_L \cdot a \cdot \chi_{\mathrm{detach}} \cdot \frac{y_{\mathrm{Cl}_2} \cdot P}{RT} + B\left(\frac{P}{n_t RT}\right)^2 \quad (5)$$

where n_t is the total number of moles of the gas. The first term of (5) represents the liquid phase processes, including Cl_2 conversion, whereas the second term reflects the gas phase deactivation mechanisms described in Table I. The first term is similar to the chlorine consumption described in (4), but with the addition of the factor χ_{detach} that describes the percentage of generated $\mathrm{O}_2(\mathrm{a})$ that appears in the gas phase. Some of the $\mathrm{O}_2(\mathrm{a})$ molecules are deactivated according to reaction R1e as they diffuse back across the 10-nm reaction depth to the liquid/gas interface; additionally, a small portion of the $\mathrm{O}_2(\mathrm{a})$ molecules that reach the liquid/gas interface diffuse back into the bulk liquid and are quenched. Several approaches to determining the detachment yield have been described in the literature [11], [12], [15]–[17]. These approaches produce similar but not identical estimates of detachment yield by describing similar mechanisms in various levels of detail. In all of these approaches, uncertainties in the physical constants (for example, as reported in [13], [15], and [18]–[21]) can result in significant uncertainties in the calculated detachment yields. In this paper, an initial estimate of the $\mathrm{O}_2(\mathrm{a})$ loss due to liquid phase deactivation was made by comparing the timescale for $\mathrm{O}_2(\mathrm{a})$ quenching in the liquid to the timescale for $\mathrm{O}_2(\mathrm{a})$ diffusion back through the reaction layer [15]. Assuming that the diffusivities of oxygen and chlorine in BHP are 10^{-5} cm^2/s, the deactivation timescale is 40 times greater than the diffusion time, suggesting a loss of about 2.5% of the $\mathrm{O}_2(\mathrm{a})$ en route to the liquid/gas interface. A more detailed approximation of χ_{detach} was obtained using the method of [11]. This approach takes into account both the deactivation by R1e and the surface detachment processes [11], [16], [17]. Using the same values for the diffusivities that are used above, this produces a χ_{detach} of 94%; alternatively, using the parameter values given in [11] would produce a χ_{detach} of 90%. These methods suggest that the detachment yield is in the range of 90%–97.5%. Although a 5% to 10% yield loss corresponds to a large difference in $\mathrm{O}_2(\mathrm{a})$ concentration in the reaction channels themselves, the change in concentration at the measurement point is only on the order of 10^{14} cm^{-3} because of gas phase deactivation. This difference is well below the detection limit of the optical emission diagnostic. As a result the model used here approximates $\chi_{\mathrm{detach}} = 1$. The coefficient B in the second term can be expressed as

$$\begin{aligned} B = & -2k_2 y_{\mathrm{O}_2(\mathrm{a})}^2 - 2k_3 y_{\mathrm{O}_2(\mathrm{a})}^2 + k_4 y_{\mathrm{O}_2(\mathrm{b})} y_{\mathrm{O}_2(\mathrm{a})} \\ & + k_5 y_{\mathrm{O}_2(\mathrm{b})} y_{\mathrm{H_2O}} + k_6 y_{\mathrm{Cl}_2} y_{\mathrm{O}_2(\mathrm{b})} + k_7 y_{\mathrm{Cl}_2} y_{\mathrm{O}_2(\mathrm{b})} \\ & + k_8 y_{\mathrm{O}_2(\mathrm{b})} y_{\mathrm{He}} - k_9 y_{\mathrm{O}_2(\mathrm{a})} y_{\mathrm{O}_2(\mathrm{b})} - k_{10} y_{\mathrm{O}_2(\mathrm{b})} y_{\mathrm{H_2O}} \\ & - k_{11} y_{\mathrm{Cl}_2} y_{\mathrm{O}_2(\mathrm{a})} - k_{12} y_{\mathrm{O}_2(\mathrm{a})} y_{\mathrm{He}} \end{aligned} \quad (6)$$

TABLE II
CHANGES BETWEEN ORIGINAL MODEL AND ACTUAL μSOG GEOMETRY

	SOG Parameters used in Wilhite et al.	Updated SOG Parameters
Cl_2 Viscosity (g/cm/s)	$2x10^{-4}$ g/cm/s	$2x10^{-4}$ g/cm/s
BHP Viscosity (g/cm/s)	$1x10^{-2}$ g/cm/s	$1.8x10^{-2}$ g/cm/s
BHP Density (g/cm^3)	1.373 g/cm^3	0.983 g/cm^3
Packing Diameter (cm)	$7x10^{-3}$ cm	$7x10^{-3}$ cm
Void fraction of packed-bed	0.40	0.45
Reaction Length (cm)	0.516	0.6

where y_x is the molar fraction of the species x, and each k coefficient is the particular reaction constant between two certain species, as given in Table I. The pressure drop across the reaction channels is modeled using the equation of Ergun [22], which is written for gases as

$$\left.\frac{dP}{dz}\right|_g = -\frac{F_t \cdot RT}{D_p \cdot P \cdot a_c} \cdot \left(\frac{1-\varepsilon}{\varepsilon^3}\right) \cdot \left[\frac{150 \cdot (1-\varepsilon) \cdot \mu_g}{D_p} + 1.75 \cdot \mathrm{MW}_g \cdot \frac{F_t^2 \cdot RT}{P \cdot a_c}\right] \quad (7)$$

where z is the distance along the reaction channel, F_t is the total molar flow rate (constant), D_p is the packing diameter in the channels, a_c is the cross-sectional area of the reaction channels, ε is the void fraction, μ_g is the viscosity of the gas, and MW_g is the molecular weight of the gas. A similar relationship between liquid flow and differential pressure drop in the reaction channels also exists. Assuming ideal plug flow in the channels, the relationship between molar flow rate F_i and species production r_i for a species i is

$$\frac{1}{\varepsilon_g \cdot a_c} \cdot \frac{d(F_i)}{dz} = r_i \quad (8)$$

where ε_g is the fraction of the volume in the reaction channels that is occupied by the gas phase. Substituting (5) into (8) yields

$$\frac{dF_{\mathrm{O}_2(\mathrm{a})}}{dz} = \varepsilon_g \cdot a_c \cdot a \cdot k_L \cdot \chi_{\mathrm{detach}} \cdot \frac{y_{\mathrm{Cl}_2} \cdot P}{RT} + \varepsilon_g \cdot a_c \cdot B\left(\frac{P}{F_t RT}\right)^2. \quad (9)$$

Similar expressions were obtained for the other reactants and reaction products. The kinetic model is discussed in more detail in [3].

Several modifications to the original model were made to analyze the data collected by the testing rig. The reactant properties, which were initially assumed to be similar to those of air and $\mathrm{H_2O}$, were modified to more accurately represent BHP and Cl_2 [23]. Additionally, the μSOG dimensions were changed to reflect the fabricated device. Table II illustrates these changes.

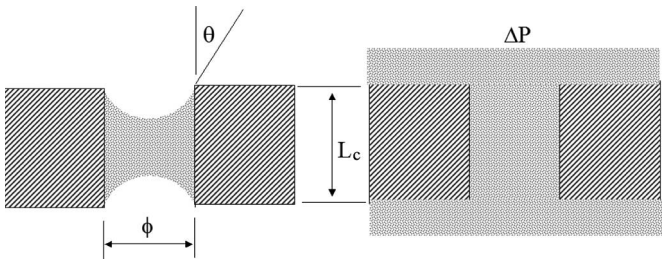

Fig. 3. Illustration of capillary pores with (left) nonzero and (right) zero wetting angles. When fully filled in, the capillaries are not surface tension driven but pressure driven.

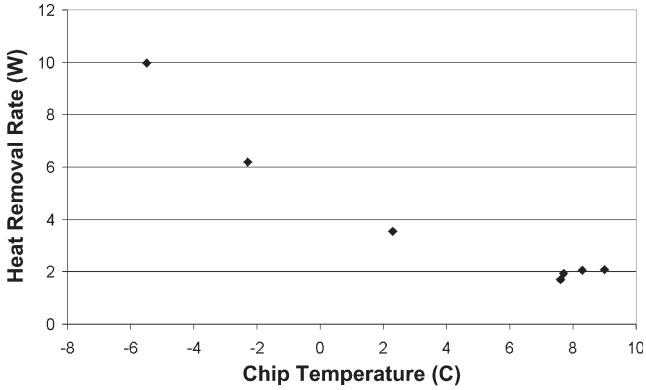

Fig. 4. Measured heat removal capacity of the microfabricated heat exchanger versus internal chip temperature. For these data, the heat source was provided by the ambient surrounding the chip package.

A. Capillary Separator Region

The model was updated to reflect the dynamics of the capillary separator region. The separator, which is first described in [24] and [25], relies on capillary action to remove the liquid waste while allowing the gas to freely pass. The wetting front of the liquid byproducts gets sucked in due to surface tension effects, thus filling in the capillary. The liquid will wet the capillary with a certain wetting angle θ (Fig. 3, left). In a steady-state flow configuration, the capillaries are fully filled in, and thus, the separator is pressure driven (Fig. 3, right). The maximum pressure drop that can exist across a capillary given a zero wetting angle is

$$\Delta P = \frac{4\Sigma}{\phi} \tag{10}$$

where Σ is the surface tension of the liquid, and ϕ is the diameter of the capillary. This value is also the maximum pressure that surface tension effects can provide to pump the liquid byproducts without the need for an external pressure signal. For 20-μm-wide capillaries and given the surface tension of water (72 dyn/cm), the maximum pressure drop that the meniscus can withstand is 108 torr. A second expression for pressure can obtained from the Hagen–Poiseuille equation if steady-state fully developed flow is assumed and the liquid is Newtonian, with pressure losses produced by viscosity. In this case, the volumetric flow rate Q through each capillary is given by [26]

$$Q = \frac{\pi \Delta P \phi^4}{128 \mu L_c} \tag{11}$$

where μ is the viscosity of the fluid, and L_c is the channel length. For a given pressure drop across the separator, the number of pores needed to transport the liquid byproducts can be found by dividing the total liquid molar flow rate Q_t by Q. Q_t is expressed as

$$Q_t = \frac{\gamma \varphi y_{\mathrm{Cl}_0}}{[\mathrm{O_2H}]} \tag{12}$$

where φ is the total gas molar flow rate, γ is the desired ratio of peroxide ions to Cl_2, and y_{Cl_0} is the chlorine fraction of the entering gas stream. The original design called for a $10:1$ peroxide ion to Cl_2 ratio and a peroxide ion concentration $[\mathrm{O_2H^-}]$ of 6.5×10^{-3} mol/cm^3. For a gas flow rate of 50 sccm, around 430 capillaries would be necessary; for a gas flow rate of 250 sccm, the number of capillaries necessary rises to about 2200. However, more than 7000 were included in the actual devices due to concerns about how many functioning pores would be produced in the deep reactive ion etching steps. In addition, it was desired to have some redundancy in the separator in case clogging occurred during testing of the chip.

B. Heat Exchanger

Because of the high enthalpy associated with the reaction, any $O_2(a)$ generation system must include a heat removal mechanism. In the μSOG, this task is accomplished using a heat exchanger composed of 19 parallel cooling channels that are directly situated beneath the reaction area. The lower silicon layer of the MEMS chip contains the microfabricated heat exchanger. The heat exchanger channels are filled with a silicone-based coolant and are connected to an external chiller. Given an enthalpy of reaction of -110 kJ/mol and a maximum Cl_2 molar flow rate of 3×10^{-5} mol/s in these experiments, the heat exchanger needs to be capable of removing at least 3.5 W of heat in order to remove the excess heat of reaction. In addition, in order to maintain the chip at a temperature that lies within BHP safety limits and restricts the amount of water vapor in the exit flow, which is important for overall COIL performance, the heat exchangers must also remove the heat that enters the chip from the ambient, which is estimated to be about 10 W for the present experimental setup and an operating temperature of $-5\,^{\circ}$C. In order to handle this task, the channels were sized at 23.9 mm in length and 300 μm wide. The heat removal capacity of the microfabricated heat exchanger was empirically verified before attempting to produce $O_2(a)$. Using thermocouples to monitor the coolant and silicon temperatures, the specific heat equation was used to calculate the total heat removed. Fig. 4 illustrates the measured heat removal capacity of the channels as a function of the silicon temperature. The heat removal capacity Ξ was calculated using the expression

$$\Xi = \dot{m} \cdot Cp \cdot \Delta T \tag{13}$$

where $\dot{m}$ is the mass flow rate of coolant, Cp is its heat capacity, and ΔT is the temperature difference across the heat exchanger.

C. Singlet Delta Oxygen Deactivation

Once $O_2(a)$ has been created, it can be deactivated both inside the μSOG chip and in the external flow paths by collisions with other $O_2(a)$ molecules (pooling reactions) and collisions with the walls of the flow path. The rates of the pooling reactions and the wall deactivation reactions depend, as described below, on the geometry and material composition of the chip's internal gas exit path and the external flow path. The chip's internal exit flow path has a length of 1.8 cm and a width of 2 mm, and its surface is silicon-rich silicon nitride, as described in Part I. Upon exiting the chip, the gas mixture flows into a quartz cuvette. The cuvette's inlet is a 1-cm-long tube with an inner diameter of 2 mm, and it is connected by a 0.5-cm-long transition region to a diagnostic region that has a 1×1-cm square cross section. The rectangular portion features 1-mm-thick walls.

The mole fraction $y_{O_2(a)}$ of $O_2(a)$ in a rectangular volume as a function of flow length can be described as

$$\frac{dy_{O_2(a)}}{dl} = \frac{-(2k_3+k_2)P}{RTv_{gas}} y^2_{O_2(a)} - \psi_w \frac{(W+H)}{2WH}\sqrt{\frac{8RT}{\pi(MW_{O_2})}}\, y_{O_2(a)} \quad (14)$$

where P is the total pressure of the gas, R is the universal gas constant, T is the gas temperature, v_{gas} is the flow velocity, W is the width of the flow path, H is the height of the flow path, (MW_{O_2}) is the molecular weight of oxygen, ψ_w is the $O_2(a)$ deactivation coefficient for the particular wall material, and l is the dimension along the flow axis. The first term of (14) derives from the reactions described in (6); only the dominant terms are kept, and the rate of reaction 5 is taken to be large enough to make the net effect of reaction 2 be the deactivation of a single $O_2(a)$ molecule. Equation (14) is the well-known Ricatti equation [27], which has the general form

$$\frac{du(l)}{dl} + \Lambda(l)\cdot u(l) + \Theta(l)\cdot u^2(l) = \Omega(l) \quad (15)$$

where $u(l)$ is the function, and l is the independent variable. The transformation

$$u(l) = \frac{dw(l)}{dl} / \left[\Theta(l)\cdot w(l)\right] \quad (16)$$

converts the nonlinear differential equation into the following homogeneous linear second-order ordinary differential equation:

$$\frac{d^2w(l)}{dl^2} + \left[\Lambda(l) - \frac{d\Theta(l)}{dl}/\Theta(l)\right]\cdot\frac{dw(l)}{dl} + \cdot\Omega(l)\cdot\Theta(l)\cdot w(l) = 0. \quad (17)$$

For the particular case of (14), the following equations were derived:

$$\Lambda(l) = \Lambda = \psi_w \frac{(W+H)}{2WH}\sqrt{\frac{8RT}{\pi MW_i}} \quad (18)$$

$$\Theta(l) = \frac{(2k_3+k_2)P}{RTv_{gas}} \quad \frac{d\Theta(l)}{dl} = 0 \quad \Omega(l) = 0. \quad (19)$$

Therefore, (17) simplifies to

$$\frac{d^2w(l)}{dl^2} + \Lambda\cdot\frac{dw(l)}{dl} = 0. \quad (20)$$

The solution of (20) is

$$w(l) = C_1 e^{-\Lambda\cdot l} + C_2 \quad (21)$$

where C_1 and C_2 are integration constants. Substituting (21) into (16), and applying the initial condition that $y_{O_2(a)}(l = 0) = y_0$, which is the initial mole fraction of $O_2(a)$, the solution of (14) is

$$y_{O_2(a)}(l) = \frac{y_0}{\left[y_0\cdot\frac{\Theta}{\Lambda}+1\right]\cdot e^{\Lambda\cdot l} - y_0\cdot\frac{\Theta}{\Lambda}} \quad (22)$$

It can be quickly verified that $y_{O_2(a)}(l \longrightarrow \infty) = 0$ and that $y_{O_2(a)}(l \geq 0) > 0$. For a very small wall deactivation coefficient so that $\Lambda * 1 \ll 1$ and $e^{\Lambda * l} \cong 1 + \Lambda * l$, (22) simplifies to

$$y_i(l) = \frac{y_0}{1 + y_0\Theta l}. \quad (23)$$

Equation (23) was used to determine the $O_2(a)$ concentration and yield-utilization product at the chip's $O_2(a)$ gas outlet from the measured values in the diagnostic region of the quartz cuvette.

According to (23), most of the $O_2(a)$ is expected to have returned to the ground state by the time it reaches the measurement point, with pooling losses expected to dominate. In a real MEMS-based COIL, however, the mole fraction of $O_2(a)$ is expected to be much higher at the point at which the iodine flow is injected in order to produce the lasing effect. In the present experiments, the significant deactivation that takes place before the measurements are made is a function of the scale mismatch between the μSOG and the macroscale diagnostic region, which results in a small value for v_{gas}. In a scaled-up system of many arrayed μSOGs, the higher $O_2(a)$ flow rates will increase v_{gas} and greatly reduce the deactivation as compared with the present experiments. Although some deactivation will still occur, it is expected that the amount of deactivation between the point of $O_2(a)$ production and the chip's exit port in the present experiments will be a better predictor of the deactivation that will occur in the internal flow paths that will ultimately connect the μSOGs to the rest of the MEMS COIL system.

V. Experimental Procedure

The first step in the experiment is to prepare the BHP solution, which consists of equal parts 50 wt% aqueous KOH solution and 50 wt% H_2O_2. The external chiller is set at -20 °C,

with the aim of the coolant reaching the rig at a temperature of -15 °C. The KOH solution was prepared by dissolving KOH pellets (Mallinckrodt, Phillipsburg, NJ) in deionized water. The KOH and H_2O_2 were slowly mixed together to ensure that the temperature never exceeded 25 °C. BHP and He flow were first initiated in the chip at atmospheric pressures. Gas and liquid flow were immediately visible in the reaction channels, and the capillary separator correctly functioned at the outset. The set points of the pressure controllers were then gradually lowered until the desired operating points were reached. The coolant flow was then started and increased until it reached its set point at around -5 °C. Once the set points of pressure and temperature had been reached, the chlorine, which is flowing concurrently with helium with a 3 : 1 ratio of He to Cl_2, was injected into the chip in pulses that were typically 1 min in length. The photonic emission coming out of the exit flow was measured using the spectrometric setup previously described, and the gas products were analyzed using a commercial mass spectrometer. After a number of runs, the remaining BHP was collected, and then the chip was warmed up (the coolant flow was stopped) while deionized water was flowed to ensure chip reutilization. After a few minutes of water flow, the chip was dismounted from the package, dried out using an oven, and stored for future use. Data were taken at 15 different operating points. The plenum pressure ranged from 50 to 200 torr, and the total gas flow rate varied between 50 and 200 sccm. Crystals of KCl were observed to form in the device channels after a number of runs (and in particular, after runs with very high ratios of chlorine gas to BHP) and eventually led to clogging in the device channels. The clogging, in turn, lessened the intensity of the spectral peaks with successive chlorine pulses. The implications of the observed clogging for the μSOG's utility and for the analysis of the results are further discussed in Section VII. It was also observed that very little of the capillary separator area appeared to be used in removing waste products, as expected from the considerable oversizing of the separator, as described earlier. This experimental fact will be important when discussing the $O_2(a)$ yield and will also be discussed further in Section VII.

VI. Steady-State Validation and Dimol Emission Characterization

Confirmation of the steady-state operation of the chip was achieved by using two different diagnostics. The first diagnostic was measurement of the IR spectra. The IR spectra were recorded to monitor the $O_2(a \longrightarrow X)$ transition, starting from the moment the chlorine plug was delivered to the chip. A typical set of IR spectra is shown in Fig. 5. Each spectral curve is obtained with a 5-s integration time. It is clear from Fig. 5 that the device quickly reaches steady-state operation after the chlorine pulse is started. It can also be seen that there is some minor production of $O_2(a)$ after stopping the chlorine delivery, probably due to the nonidealities of the testing setup (dead volume within the pipes, nonperfect seal of the mass flow meters, etc.). The increase in intensity after scan 20 is due to a reduction in the He flow rate, which in turn increased the Cl_2 residence time in the inlet lines. Each of the IR spectra (Fig. 6)

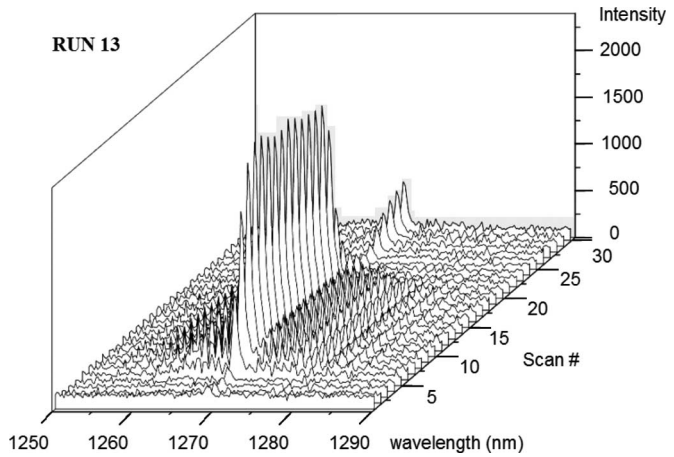

Fig. 5. IR emission spectra from the μSOG versus time for a single 1-min chlorine pulse. The spectral intensity is given in arbitrary units.

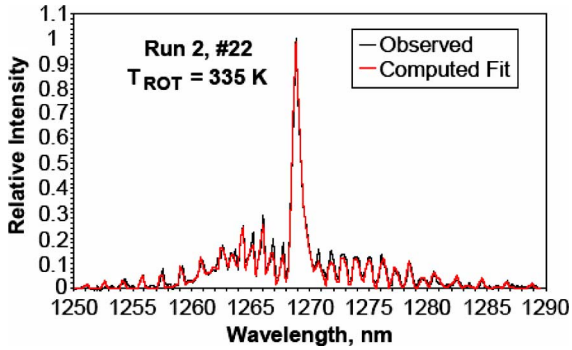

Fig. 6. Typical IR spectra for a 5-s integration time. A least-squares fit was used to calculate the $O_2(a)$ temperature. The typical temperature falls in the 295–335-K range, in contrast with the subzero temperature of the chip.

shows the characteristic molecular band structure of the emission transition from $O_2(a^1\Delta_g, v = 0)$ to $O_2(X^3\Sigma_g^-, v = 0)$, with a prominent Q-branch at the band center and weaker rotational branches on each side. Spectroscopic analysis of the detailed band shape gives the rotational temperature of the $O_2(a)$, which is the same as the gas temperature for these conditions [10]. It is interesting to observe that although the chip is kept below 273 K, the $O_2(a)$ at the detection point is at temperatures above 300 K. It is likely that the gas is warmed by a combination of conduction from the room-temperature optical measurement cell and energy released from the $O_2(a)$ pooling reactions.

Fig. 7 shows the dimol spectra of multiple runs. It can be seen that the spectrum is centered on two peaks (one each at 634 and at 703 nm), as expected from the known behavior of the dimol emission.

The second approach in determining the steady-state operation of the device used the mass spectrometer data (Fig. 8). The figure clearly shows a rise in the O_2 partial pressure roughly corresponding to the Cl_2 pulse. The increase in O_2 partial pressure appears approximately constant during the Cl_2 pulse, given the time-averaging effects of the long time constant for transport through the sampling capillary, thus indicating

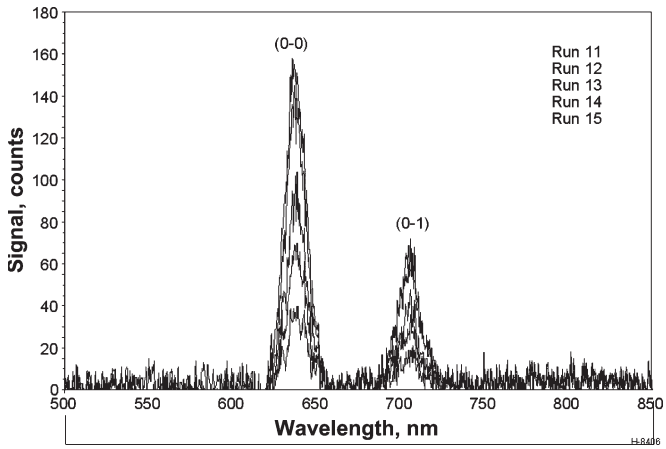

Fig. 7. Spectra resulting from dimol emission.

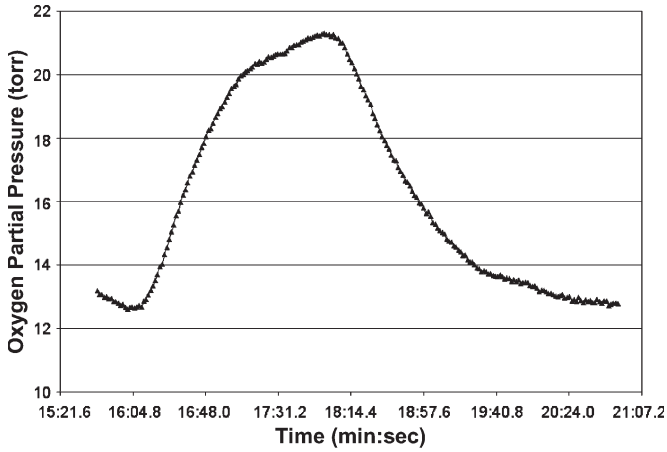

Fig. 8. Typical mass spectrometer data for a 2-min chlorine pulse run.

steady-state operation. Attempts at quantitatively measuring the increase in O_2 mole fraction with mass spectrometry were hampered by limitations in the testing rig. Specifically, the low temperature of the LN_2 traps condensed out much of the O_2 in the gas stream along with the Cl_2. The mass spectrometry therefore substantially underestimated the O_2 production, as evidenced by the fact that the amount of $O_2(a)$ detected by IR spectrometry at the measurement point (even without taking into account deactivation losses) sometimes exceeded the amount of total O_2 detected in the outlet flow by mass spectrometry.

The steady-state production of $O_2(a)$ masks an intricate fluid dynamics process, as shown in Fig. 9, where trickling rather than plug flow was observed in the reaction channels.

VII. Data Analysis: $O_2(a)$ Yield, Chlorine Utilization, and Flow Power

The $O_2(a)$ emission spectra were corrected for instrumental baseline and for the absolute spectral responsivity using the blackbody calibration results. The corrected spectra were integrated over the entire molecular band to determine the volumetric photon emission rate within the field of view. When

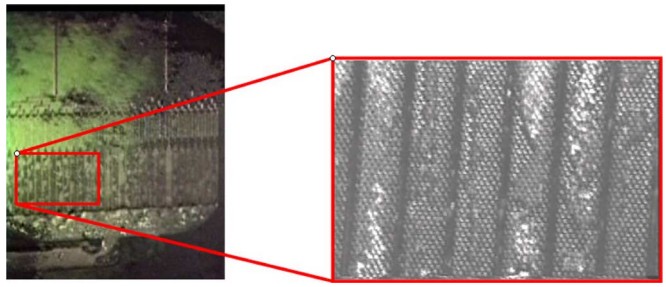

Fig. 9. Trickling flow was observed in the reaction channels.

this value is divided by the Einstein coefficient, which represents the rate at which $O_2(a)$ molecules decay into the $O_2(X)$ state ([28], [29]), the concentration of $O_2(a)$ is determined [10]. This concentration is an average over the field of view. The μSOG emission measurements were taken near the center of the quartz cuvette attached to the package, at a distance of approximately 3.05 cm from the gas outlet of the chip. Table III summarizes the conditions for each run, along with the measured concentrations at each point. The error in the measurements, around 13% for each run, results from uncertainty in the Einstein coefficient (10%) as well as from small uncertainties in the geometry of the setup. The measured $O_2(a)$ concentrations range from 5×10^{16} to 1×10^{17} cm^{-3}. The yield-utilization product, or the fraction of O_2 in the $O_2(a)$ state assuming 100% Cl_2 utilization, is also given in Table III. Ideally, the $O_2(a)$ concentration would be measured at the gas outlet, since that is the point at which the next stage of the laser system would be connected. Measurements are made further down the cuvette in this case in order to ensure that the field of view of the collimated optics is not obscured by the package or other parts of the test apparatus. Fortunately, (23) can be used to extrapolate the $O_2(a)$ concentration and yield-utilization product anywhere along the flow path given a concentration value downstream from that point, albeit with increasingly larger error bars. In this analysis, (23) is used to extrapolate the measured concentration and yield-utilization product up to the chip's gas outlet. As was mentioned above, the values at the chip's outlet are expected to be a better predictor of the performance of the μSOG chip in a complete MEMS COIL system than the value at the current measurement point is. The scale mismatch between the μSOG and the external diagnostic region in this case leads to low flow velocities and much greater $O_2(a)$ losses than would occur in a MEMS COIL system in which the components were integrated at the MEMS scale. When the measured values are extrapolated to the chip's outlet using (23), the resulting values are substantially higher, with yield-utilization products approaching 80% and with the concentrations in most runs in excess of 10^{17} cm^{-3}.

When the yield-utilization products extrapolated from the raw data were compared with those predicted by the baseline kinetics model described above, it became evident that some modification to the baseline model would be necessary in order to adequately explain the results. In most of the experimental runs, the extrapolation of the measured data produced higher but plausible values of the concentration and yield-utilization

TABLE III
SUMMARY OF μSOG MEASUREMENTS

Run	He, (sccm)	Cl_2, (sccm)	BHP Flow Rate (cm^3/min)	P_{plenum}, (torr)	$O_2(^1\Delta)$ Temp., (K)	Measured conc., ($x10^{17}$ cm^{-3}) (+/-13%)	Measured yield-utilization product	Extrapolated initial conc., ($x10^{17}cm^{-3}$)	Extrapolated initial yield-utilization product	Predicted initial yield-utilization product	Extrapolated Power, (W)	Molar Flow rate, ($x10^{-4}$ mol s^{-1} L^{-1})
1	37	13	0.95	100	330	0.72	0.095	5.13 +2.19/-2.65	0.7011 +0.3/-0.36	0.7057	0.615 +0.3/-0.32	299 +144.7/-154
2	56.75	18.75	1.32	100	335	1.04	0.144	5.64 +1.57/-2.52	0.78 +0.22/-0.35	0.7674	1.02 +0.29/-0.46	500 +140/-224
3	75	25	1.31	100	335	0.95	0.132	2.15 +0.76/-0.54	0.2987 +0.105/-0.08	0.7991	0.52 +0.19/-0.132	255 +90/-64
4	37	13	0.95	100	330	0.76	0.10	$\geq$ 3.14	> 0.4292	0.7057	$\geq$ 0.376	> 183
5	56.75	18.75	1.32	100	320	0.72	0.096	1.76 +0.69/-0.47	0.23 +0.091/-0.062	0.7628	0.306 +0.12/-0.08	149 +58/-40
6	75	25	1.29	200	325	0.85	0.057	$\geq$ 7.14	> 0.4809	0.6295	$\geq$ 0.843	> 410
7	75	25	1.30	150	335	1	0.091	8.48 +2.33/-4.74	0.7845 +0.2155/-0.4385	0.7225	1.37 +0.379/-0.769	669 +184/-374
8	93.75	31.25	1.30	100	333	0.92	0.126	1.63 +0.42/-0.34	0.2248 +0.0575/-0.0470	0.8154	0.494 +0.125/-0.102	240 +61/-50
9	112.5	37.5	1.29	100	310	0.77	0.099	1.14 +0.24/-0.21	0.1468 +0.0302/-0.0266	0.8185	0.387 +0.08/-0.07	188 +39/-34
10	131.25	43.75	1.29	100	305	0.77	0.097	1.08 +0.21/-0.19	0.1359 +0.0260/-0.0235	0.82	0.418 +0.08/-0.072	203 +39/-35
11	125	25	1.29	100	300	0.86	0.159	1.38 +0.31/-0.27	0.2566 +0.0581/-0.0496	0.8568	0.451 +0.102/-0.09	219 +50/-42
12	175	25	1.28	100	285	0.7	0.167	0.92 +0.17/-0.15	0.2180 +0.039/-0.0359	0.8771	0.383 +0.067/-0.064	186 +33/-31
13	75	25	1.32	50	300	0.9	0.225	1.28 +0.25/-0.22	0.3175 +0.062/-0.056	0.8487	0.558 +0.109/-0.097	271 +53/-47
14	75	25	1.32	50	298	0.95	0.232	1.39 +0.28/-0.25	0.342 +0.068/-0.061	0.8485	0.601 +0.121/-0.107	292 +59/-52
15	37	13	1.34	50	295	0.5	0.116	0.75 +0.16/-0.14	0.1835 +0.383/-0.034	0.8039	0.160 +0.32/-0.03	78 +16/-14

product; however, in four of the runs, the extrapolation produced values of concentration and yield-utilization product that were not possible. In those four cases, the extrapolation indicated that there was more than one $O_2(a)$ molecule appearing at the chip's gas outlet for each Cl_2 molecule that entered at the input, which is not possible. In some of these cases, even extrapolating the lower error bar for the measurement point produced unphysically high values for $O_2(a)$ concentration at the chip's outlet.

Three sources of error were identified as possible contributors to the discrepancy. The first is clogging in the pressure drop and reaction channels, which is caused by KOH crystal precipitation and KCl salting, respectively. The second is the possibility that some of the output gas was sucked through open pores in the capillary separator rather than exiting through the gas outlet. The third is the documented uncertainty in the kinetics rate coefficients k_2 and k_3 that appear in the Θ coefficient in (23) [30]. Each of these three error mechanisms is discussed below; it will be seen that only the uncertainty in the pooling rate coefficients provides an adequate explanation of the discrepancy between the baseline model and the results.

Clogging of the flow channels was observed under two general conditions: when the chip had been operated for long periods of time with moderately high ratios of chlorine to BHP

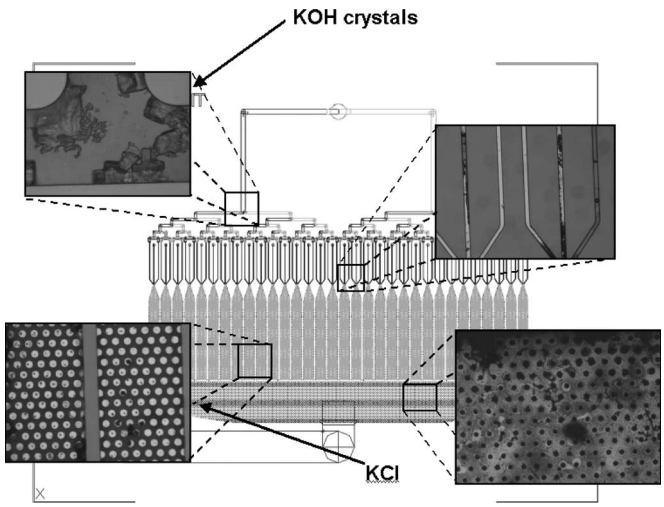

Fig. 10. SOG diagram overlaid with optical microscope images showing clogging due to (top) KOH precipitation and (bottom) KCl clogging.

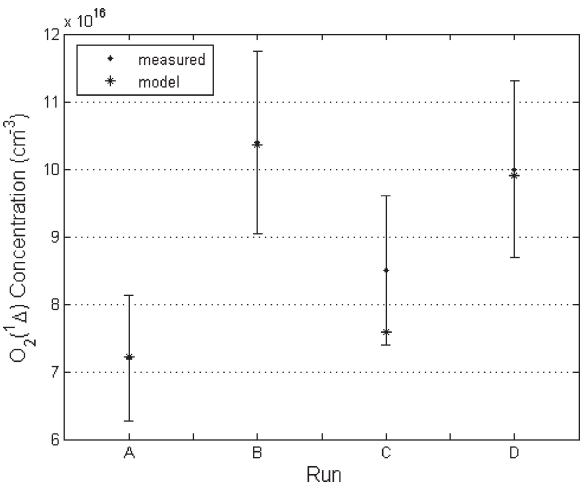

Fig. 11. Model fit for the highest confidence runs. Best agreement between measured and predicted yield-utilization product at measurement point occurs when the pooling coefficient is scaled by 0.845.

and when the chip had been operated even for short times with particularly high ratios of chlorine to BHP. During operation, clogging was evidenced by a pressure rise on the gas feed lines for a given mass flow rate of feed gas. It is not surprising that clogging occurred in some of the runs. The μSOG was designed to operate with a ratio of BHP to chlorine that corresponds to a $10:1$ ratio of peroxide ions to chlorine as compared with a many tens to one ratio that is used to prevent clogging in macroscale SOGs; a lower ratio corresponds to more efficient reactant usage. In practice, in these experiments, the chip was usually operated with a ratio of peroxide ions to chlorine in the range of approximately 3.7–13. It is reasonable to expect that some clogging would occur under these conditions, and to expect that increasing the BHP flow rate by a factor of 2 for a given chlorine flow rate would reduce or eliminate the clogging. The occurrence of clogging in some conditions and not in others also means that some of the runs may be considered to be a better indication of clog-free operation than others. In general, the most reliable data are considered to be the data that meet the following three criteria: they were taken toward the beginning of a given day's measurements, they were taken at higher ratios of peroxide ion to chlorine, and there was no significant rise in gas feed pressure observed for given mass flow rate. When the 15 runs were judged according to these criteria, the four runs that yielded unphysically high extrapolated values of $O_2(a)$ at the chip's outlet were found to suffer from minimal clogging. It is therefore expected that clogging will not provide an explanation for the observed discrepancy. In addition, the expected effect of clogging is not to increase the concentration of $O_2(a)$ at the chip's outlet, but rather to decrease it. For a given mass flow rate set by the mass flow controllers, the effect of clogged channels like those shown in Fig. 10 is to increase the gas and liquid velocities within the remaining channels. This reduces the reactants' residence time in the channels so that less $O_2(a)$ would be produced. Since the observed discrepancy is in the other direction (anomalously high concentrations), and since the runs with anomalously high concentrations are relatively free of clogging, clogging is rejected as an explanation for the observed discrepancy.

The second two potential sources of error (loss of $O_2(a)$ through the capillary separator and error in the pooling rate coefficients) were assessed by including them in a revised μSOG model and assessing whether including these effects could remove the discrepancy. In order to ensure that clogging was not affecting the comparison between model and experiments, the comparison was made for the four runs that were deemed to be the most free of clogging and for which the discrepancy was the largest. Two revisions to the baseline model were necessary. A fluidic circuit analogy was used to estimate the percentage of gas that was sucked through the separator holes along with the liquid waste. The fluidic circuit assumes incompressible fully developed flow in both the liquid and gas phases with a variable number of open holes N. The resulting loss of gas through the liquid separator is then accounted for in the calculation of the flow rates in the gas exit flow path. The model was also modified to account for the uncertainty of the pooling rate coefficients by making the effective pooling rate coefficient $2k_3 + k_2$ (or equivalently, Θ) a variable parameter. In order to determine the best values for Θ and N, both parameters were independently varied, and the sum of squared errors between the model's predicted concentrations at the measurement point and the measurements themselves were calculated for the four highest confidence runs. The best agreement between the kinetics model and the measured data, as shown in Fig. 11, occurred when $2k_3 + k_2$ was set at 84.5% of the published value, and gas leakage through the capillary separator was negligible. These corrected values for the rate coefficients fall within the error bars of the cited source reference for the kinetic constants [30]. Fig. 12 shows a pronounced drop in the error as the scalar multiplier of Θ is varied. This is not a unique minimization in the 2-D (Θ, N) space. Similar minima are obtained for nonzero values of N, but they correspond to still smaller values of the pooling rate coefficient. The best agreement occurs (and minimum modification to $2k_3 + k_2$ is necessary) when N approaches zero, suggesting that the occasional gas bubbles that were observed flowing through the separator's liquid outlet line

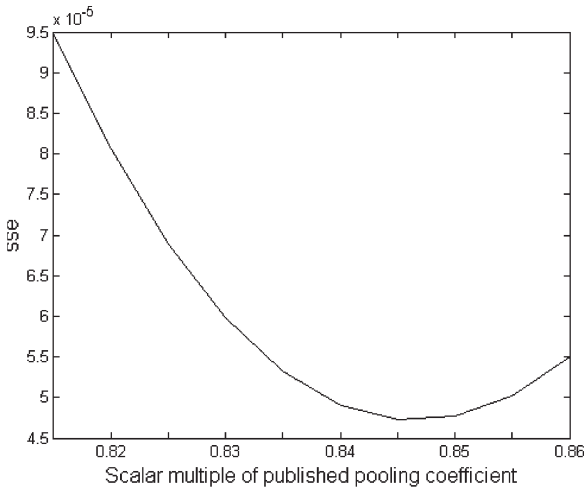

Fig. 12. Minimum square error sum versus scalar multiple of Θ for the data set with the highest confidence level. There is a range of possible kinetic constants and $O_2(a)$ separator leak that yield equivalent minimum error, but all combinations point toward small $O_2(a)$ bleed.

had a negligible effect on the measurement. In other words, if significant $O_2(a)$ flows were sucked in by the separator, the flow velocity in the gas outlet would be still smaller. As a result, k_2 and k_3 would also need to be even smaller to give physically meaningful predictions at the chip's $O_2(a)$ outlet. However, it is possible to have a small $O_2(a)$ separator leak and still have pooling rate coefficient values that fall within the error bars of the reference and essentially yield the same minimum error.

As was described before, only a small fraction of the separator seems to be covered by the wetting front of the liquid byproducts. Given the pressure difference applied across the capillary separator, even a small number of capillaries (5% of the total number) that were not filled with liquid would have been enough to suck in all the $O_2(a)$ and prevent any observation of $O_2(a)$ at the measurement point. The experimental performance suggests that the separator worked as designed, and the capillaries that did not appear to be used during operation were nonetheless plugged with a stationary film of BHP that was put in place when BHP was first flowed through the chip. In all cases, the pressure difference across the separator is not enough to overcome the surface tension effects and clear the capillaries of liquid to allow for penetration of gas into the liquid exit flow.

The adjusted values for the pooling rate coefficients were used to calculate molar flow rates per unit of reactor volume and power in the $O_2(a)$ flow as well as yield-utilization product and $O_2(a)$ concentration at the chip's gas outlet. These values are also shown in Table III. The maximum yield-utilization product at the chip's gas outlet is determined to be 78% ($+21\%$ and -43%). This is theoretically consistent with a chlorine utilization of 100% and a yield of 78%, a chlorine utilization of 78% and a yield of 100%, or anywhere between. The lack of quantitative mass spectrometer data makes independent determination of the yield and chlorine utilization impossible. However, given that some pooling losses must have taken place between the end of the reaction channels and the chip's gas outlet, it is reasonable to conclude that this corresponds to a chlorine utilization of near 100% and a yield of about 78%.

TABLE IV
COMPARISON OF THIS PAPER WITH OTHER REPORTED SOG TECHNOLOGIES ([31], [33], [35], [36])

SOG Type	Molar Flowrate (mol s^{-1} L^{-1})x10^{-4}
Sparger	2.3
Disk-Type	87
Jet-Type [Zagidullin]	1670
Jet-Type [Rybalkin]	1323
μSOG (this work)	669

This yield is in line with state-of-the-art jet SOGs, which have been reported to perform with yields as high as 73% [31], [32]. High yield is particularly important in COIL reactors because some $O_2(a)$ is consumed in the dissociation of I_2 and, of the remainder, only $O_2(a)$ above the threshold yield of about 7% can contribute at all to laser output in a COIL system; incremental increases above the onset of lasing offer significant increases in power because of the dynamics of the COIL system.

A comparison of $O_2(a)$ molar flow rate per unit volume between the μSOG and other technologies is given in Table IV. The maximum molar flow rate of $O_2(a)$ per unit reactor volume is about 670×10^{-4} mol/L/s. This value includes that part of the volume of the MEMS chip that hosts the manifolds, reaction channels, and capillary separator; it does not include any volume that is solely devoted to single-chip packaging or the volume that is devoted to chip cooling. This favorably compares with the molar flow rate of $O_2(a)$ per unit of internal reactor volume for various types of published SOGs, as reported in the literature. The molar flow rate per unit of internal reactor volume for modern jet SOGs is about 1300–1700×10^{-4} mol/L/s [31], [33], nearly three times as large as the molar flow rate per unit of reactor hardware volume reported here for the μSOG chip. However, it should be noted that the μSOG volume includes the bifurcated BHP inlet as well as some of the surrounding silicon, whereas the jet SOG values only take the internal reaction volume into account.

The power carried by the flow of $O_2(a)$ at the μSOG's gas outlet may be estimated from the molar flow rate extrapolated to the gas outlet and the energy of the $O_2(a \longrightarrow X)$ transition. The resulting values for power in the flow are reported in Table III. The maximum per chip power in the output flow is 1.37 W. However, only part of the power in the $O_2(a)$ flow would be converted to laser output power if μSOG chips were used to drive a COIL system. Assuming a threshold yield of 7% and a typical COIL power extraction efficiency of 80% [34], the power in each μSOG's $O_2(a)$ flow is predicted to source about 1 W of laser output power when integrated into an appropriate COIL system. The original μSOG study [3] had proposed using arrays of microdevices to construct COIL systems with power levels ranging from several kilowatts to 100 kW. In that study, each μSOG chip was predicted to drive 2.3 W of this power output. The maximum power capability of 1.37 W per chip demonstrated in the present experiments is in agreement with the model predictions but is somewhat less than the optimum of 2.3 W per chip as identified in the initial modeling study. The difference between the predicted optimum performance and the performance demonstrated in the first μSOG chips is

not surprising, given that the chips have not yet been operated at their optimum operating point because of flow limitations in the initial test rig. It is expected that the performance of the μSOG chips will approach the predicted optimum performance more closely as they are demonstrated closer to their optimum operating point. In particular, it is expected that the output of $O_2(a)$ per chip will increase and that clogging will decrease when the chips are operated at higher BHP and chlorine flow rates and at higher BHP to chlorine ratios.

VIII. Conclusion

Generation of $O_2(a)$ using a MEMS SOG has been successfully demonstrated. The devices were tested over a range of operating points, resulting in $O_2(a)$ molar flow rates in excess of 600 mol/L/s and a yield-utilization product approaching 80%. On both of these crucial metrics, the μSOG showed performance that favorably compares with the macroscaled SOGs that are described in the published literature. Future work includes testing multiple μSOGs in tandem at their optimal operating conditions and using arrays of μSOGs to drive a MEMS COIL system.

Acknowledgment

The authors would like to thank J. Letendre for his expertise in building the experimental apparatus and D. Park for help with the images. The views and conclusions contained in this document are those of the authors and should not be interpreted as representing the official policies, either expressed or implied, of the Defense Advanced Research Projects Agency or the U.S. Government.

References

[1] G. Ruiz-Ibanez and O. Sandall, "Kinetics for reactions between chlorine and basic hydrogen peroxide," *Ind. Eng. Chem. Res.*, vol. 30, pp. 1105–1110, 1991.

[2] S. C. Tidwell *et al.*, "Scaling CW diode-end-pumped Nd:YAG lasers to high average powers," *IEEE J. Quantum Electron.*, vol. 24, no. 4, Apr. 1992.

[3] B. A. Wilhite *et al.*, "Design of a MEMS-based microchemical oxygen-iodine laser (μCOIL) system," *IEEE J. Quantum Electron.*, vol. 40, no. 8, pp. 1041–1055, Aug. 2004.

[4] L. F. Velásquez-García, T. F. Hill, B. A. Wilhite, K. F. Jensen, A. H. Epstein, and C. Livermore, "A MEMS singlet oxygen generator—Part I: Device fabrication and proof of concept demonstration," *J. Microelectromech. Syst*. to be published.

[5] T. F. Hill, L. F. Velasquez-Garcia, B. A. Wilhite, A. H. Epstein, K. F. Jensen, and C. Livermore, "A MEMS singlet oxygen generator," in *Proc. Tech. Dig. Solid-State Sensor, Actuator Microsyst. Workshop*, Hilton Head Island, SC, Jun. 4–8, 2006, pp. 114–119.

[6] W. E. McDermott *et al.*, "An electronic transition chemical laser," *Appl. Phys. Lett.*, vol. 32, no. 8, Apr. 1978.

[7] J. F. Hon, D. N. Plummer, P. G. Crowell, J. Erkkila, G. D. Hager, C. Helms, and K. Truesdell, "A heuristic method for evaluating COIL performance," *AIAA J.*, vol. 34, no. 8, pp. 1595–1603, 1996.

[8] S. J. Arnold *et al.*, "Some new emission bands of molecular oxygen," *J. Chem. Phys.*, vol. 40, no. 6, pp. 1769–1770, Mar. 1964.

[9] D. J. Bernard and N. R. Pchelkin, "Measurement of $O_2(^1\Delta)$ content in the gaseous effluents of a chemical generator," *Rev. Sci. Instrum.*, vol. 49, no. 6, pp. 794–796, Jun. 1978.

[10] W. T. Rawlins, S. Lee, W. J. Kessler, and S. J. Davis, "Observations of gain on the $I(^2P_{1/2} \rightarrow {}^2P_{3/2})$ transition by energy transfer from $O_2(a^1\Delta_g)$ generated by a microwave discharge in a subsonic flow reactor," *Appl. Phys. Lett.*, vol. 86, no. 5, p. 051 105, Jan. 2005.

[11] G. Watanabe *et al.*, "Modeling of crossflow jet-type singlet oxygen generator," *J. Appl. Phys.*, vol. 97, no. 11, p. 114 905, Jun. 2005.

[12] D. A. Copeland *et al.*, "Two-phase model of $O_2(^1\Delta)$ production with application to rotating disk generators," *Proc. SPIE*, vol. 1871, pp. 203–228.

[13] M. V. Zagidullin *et al.*, "Highly efficient jet $O_2(^1\Delta)$ generator," *Sov. J. Quantum Electron.*, vol. 21, no. 7, pp. 747–753, 1991.

[14] P. V. Avizonis and K. A. Truesdell, "The chemical oxygen-iodine laser (COIL)," *Proc. SPIE 2502*, p. 180, 1994.

[15] W. J. Thayer, A. K. Cousins, and R. D. Romea, "Modeling of uniform droplet singlet oxygen generators," *Proc. SPIE*, vol. 2117, pp. 71–100, 1994.

[16] B. D. Barmashenko and S. Rosenwaks, "Theoretical modeling of chemical generators producing $O_2(^1\Delta)$ at high pressure for chemically pumped iodine lasers," *J. Appl. Phys.*, vol. 73, no. 4, pp. 1598–1611, Feb. 1993.

[17] D. A. Copeland *et al.*, "Exact and approximate solutions of the utilization and yield equations for $O_2(^1\Delta)$ generators," *Proc. SPIE*, vol. 2119, pp. 27–41, 1994.

[18] R. J. Richardson, C. E. Wiswall, P. A. G. Carr, F. E. Hovis, and H. V. Lilenfeld, "An efficient singlet oxygen generator for chemically pumped iodine lasers," *J. Appl. Phys.*, vol. 52, no. 4962, pp. 4962–4969, Aug. 1981.

[19] G. Ruiz-Ibanez *et al.*, "Solubility and diffusivity of oxygen and chlorine in aqueous hydrogen peroxide solutions," *J. Chem. Eng. Data*, vol. 36, no. 459, pp. 459–466, Oct. 1991.

[20] N. G. Basov, M. V. Zagidullin, V. I. Igoshin, V. A. Katulin, and N. L. Kupriyanov, *Chemical Lasers*. Berlin, Germany: Springer-Verlag, 1990.

[21] O. Aharon, A. Elior, M. Herskowitz, E. Lebiush, and S. Rosenwaks, "$O_2(^1\Delta)$ generation in a bubble column reactor for chemically pumped iodine lasers: Experiment and modeling," *J. Appl. Phys.*, vol. 70, no. 10, pp. 5211–5220, Nov. 1991.

[22] S. Ergun, "Fluid flow through packed columns," *Chem. Eng. Prog.*, vol. 48, no. 2, pp. 89–94, 1952.

[23] V. V. Bakshin *et al.*, "Investigation of physical properties of basic hydrogen peroxide solutions for use in singlet oxygen generators," *Proc. SPIE 3574*, pp. 577–583, 1998.

[24] A. Gunther *et al.*, "Micromixing of miscible liquids in segmented gas–liquid flow," *Langmuir*, vol. 21, no. 4, pp. 1547–1555, 2005.

[25] J. G. Kralj, H. R. Sahoo, and K. F. Jensen, "Integrated continuous microfluidic liquid–liquid extraction," *Lab. Chip*, vol. 7, no. 2, pp. 256–263, Feb. 2007. DOI:10.1039/b610888a.

[26] V. L. Streeter, E. B. Wylie, and K. W. Bedford, *Fluid Mechanics*, 9th ed. New York: McGraw-Hill, 1998.

[27] C. M. Bender and S. A. Orszag, *Advanced Mathematical Methods for Scientists and Engineers*. New York: Springer-Verlag, 1999.

[28] S. M. Newman *et al.*, "Integrated absorption intensity and Einstein coefficients for the $O_2(a^1\Delta_g) - (X^3\Sigma_g)$ (0,0) transition: A comparison of cavity ringdown and high resolution Fourier transform spectroscopy with a long-path absorption cell," *J. Chem. Phys.*, vol. 110, no. 22, pp. 10 749–10 757, Jun. 1999.

[29] W. J. Lafferty *et al.*, "Rotational line strengths and self-pressure-broadening coefficients for the 1.27-μm, $a^1\Delta_g - X^3\Sigma_g^-$, $v = 0-0$ band of O_2," *Appl. Opt.*, vol. 37, no. 12, pp. 2264–2270, Apr. 1998.

[30] H. V. Lilenfeld, "Oxygen-iodine laser kinetics," Air. Force Res. Lab., Kirtland Air Force Base, Albuquerque, NM, AFWL-TR-83-01, 1983.

[31] V. Rybalkin *et al.*, "Parametric study of a highly efficient chemical oxygen-iodine laser with supersonic mixing of iodine and oxygen," *J. Appl. Phys.*, vol. 98, no. 2, p. 0213106, Jul. 2005.

[32] S. C. Hurlock, "COIL technology development at Boeing," *Proc. SPIE*, vol. 4631, pp. 101–115, 2002.

[33] M. V. Zagidullin *et al.*, "Highly efficient supersonic chemical oxygen-iodine laser with a chlorine flow rate of 10 mmol s^{-1}," *Sov. J. Quantum Electron.*, vol. 27, no. 3, pp. 195–199, 1997.

[34] G. P. Perram and G. D. Hager, "The standard chemical oxygen-iodine laser kinetic package," Air Force Weapons Lab., Kirtland AFB, NM, AFWL-TR-88-50, 1988.

[35] K. R. Kendrick *et al.*, "Determination of singlet-oxygen generator efficiency on a 10-kW class supersonic chemical oxygen-iodine laser (RADICL)," *IEEE J. Quantum Electron.*, vol. 35, no. 12, pp. 1759–1764, Dec. 1999.

[36] G. R. Kwirandt and W. O. Schall, "Basic experiments on the production of $O_2(^1\Delta)$," *Proc. SPIE*, vol. 2502, pp. 331–337, 1995.

Tyrone F. Hill received the B.S. degree in electrical engineering from the University of Illinois, Urbana-Champaign, in 2001, and the M.S. degree in electrical engineering from the Massachusetts Institute of Technology (MIT), Cambridge, in June 2004. He is currently working toward the Ph.D. degree in the Department of Electrical Engineering and Computer Science, MIT.

His research interests include MEMS fabrication techniques and optical emission diagnostics.

Luis Fernando Velásquez-García received the degree (Valedictorian of the School of Engineering, *magna cum laude*) in mechanical engineering and the civil engineering degree (Valedictorian of the School of Engineering, *magna cum laude*) from Los Andes University, Bogotá, Colombia, in 1998 and 1999, respectively, and the M.S. degree in aeronautics and astronautics and the Ph.D. degree in Space Propulsion from the Massachusetts Institute of Technology (MIT), Cambridge, in 2001 and 2004, respectively.

He was a Postdoctoral Associate with MIT's Microsystems Technology Laboratories and the Gas Turbine Laboratory in 2004, where he has been a Research Scientist since 2005. His research focuses on micro- and nanofabrication technologies applied to propulsion, analytical, and power systems. He has conducted research in micro- and nanotechnology applied to electrospray (internally and externally fed dense emitter arrays), plasma-enhanced chemical vapor deposited, carbon-nanotube-based devices, 3D packaging, mass spectrometry (quadrupole mass filters, electron impact ionizers, and field ionizers), and chemical reactors (monopropellant rockets and lasers).

Benjamin A. Wilhite received the bachelor's degree in chemical engineering from North Carolina State University, Raleigh, in 1997, and the Doctorate degree in chemical engineering from the University of Notre Dame, Notre Dame, IN, in 2003.

He is an Assistant Professor of chemical engineering with the University of Connecticut, Storrs. From 2002 to 2005, he was a Postdoctoral Research Associate and Research Scientist with the Massachusetts Institute of Technology, Cambridge. His research expertise is in chemical reaction engineering, multiphase transport, and membrane reformers and his interests focus on the development of portable chemistry systems and alternative energy processes operable from biofuels.

W. Terry Rawlins received the B.S. degree in chemistry and the B.A. degree in mathematics from the University of Texas at Austin, where he conducted undergraduate research in chemical kinetics with Prof. W. C. Gardiner, Jr., and the Ph.D. degree in chemistry from the University of Pittsburgh, Pittsburgh, PA, with Prof. Frederick Kaufman.

Since 1977, he has been with Physical Sciences Inc., Andover, MA, where he has pursued research in atmospheric chemistry, combustion dynamics, and chemical kinetics. His current research interests include the kinetics of excited-state species and applications to advanced chemical laser concepts.

Seonkyung Lee received the B.S. and M.S. degrees in chemistry from Ewha Womans University, Seoul, Korea, in 1992, and the Ph.D. degree in physical chemistry from Kyoto University, Kyoto, Japan, in 1997.

From 1997 to 2000, she was a Postdoctoral Associate with JILA, University of Colorado, Boulder. She is currently a Principal Research Scientist with Physical Sciences Inc., Andover, MA. Her research interests include electric oxygen-iodine laser and the development of laser-based optical diagnostic methods and applications.

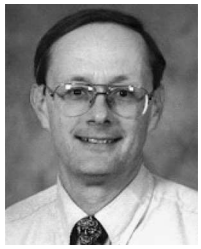

Steven J. Davis received the B.S. and Ph.D. degrees in physics from the University of New Hampshire, Durham.

He was with the Air Force Weapons Laboratory, Kirtland AFB, NM, where he led research into the development of a variety of chemical laser concepts. Since 1985, he has been with Physical Sciences Inc., Andover, MA, where he is the Executive Vice President for Applied Sciences and where he has continued his research in chemical laser development and has investigated advanced diagnostics for combustion, environmental, and medical applications.

He is a Fellow of the International Society of Optical Engineering.

Klavs F. Jensen received the M.Sc. degree in chemical engineering from the Technical University of Denmark, Copenhagen, Denmark, and the Ph.D. degree from the University of Wisconsin, Madison.

He is the Warren K. Lewis Professor and the Head of Chemical Engineering and Professor of Materials Science and Engineering with the Massachusetts Institute of Technology. His research interests include microfabrication, testing, integration, and scale-up of microfluidic systems for chemical and biochemical discovery, synthesis, and processing. Chemical kinetics and transport phenomena related to the processing of organic and inorganic materials for electronic and optical applications are also topics of interest along with the development of simulation approaches for reactive systems.

Prof. Jensen is a member of the U.S. National Academy of Engineering and a Fellow of the Royal Society of Chemistry. He serves on the Steering Committee for the International Conference on Miniaturized Systems for Chemistry and Life Sciences (μTAS) and Chair of the 2005 Conference in Boston. He received the National Science Foundation Presidential Young Investigator Award, a Guggenheim Fellowship, and the Allan P. Colburn, Charles C.M. Stine, and R.H. Wilhelm Awards of the American Institute of Chemical Engineers.

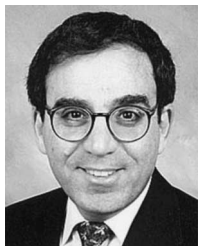

Alan H. Epstein received the S.B., S.M., and Ph.D. degrees in aeronautics and astronautics from the Massachusetts Institute of Technology (MIT), Cambridge.

He is currently the R. C. Maclaurin Professor of Aeronautics and Astronautics and Director of the Gas Turbine Laboratory at MIT. His research includes the fields of energy conversion, aero and rocket propulsion, and microsystems, specifically micropropulsion and energy conversion devices.

Dr. Epstein is a member of American Society of Mechanical Engineers (ASME), a Fellow of the American Institute of Aeronautics and Astronautics (AIAA), and a member of the National Academy of Engineering.

Carol Livermore (M'98) received the B.S. degree in physics from the University of Massachusetts, Amherst, in 1993 and the A.M. and Ph.D. degrees in physics from Harvard University, Cambridge, MA, in 1995 and 1998, respectively.

From 1998 to 2002, she was first a Postdoctoral Associate and then a Research Scientist with the Massachusetts Institute of Technology (MIT), Cambridge. She is currently the SMA Assistant Professor of manufacturing with the Department of Mechanical Engineering, MIT. Her current research interests include power MEMS and the development of techniques and applications for nano- and microscale self assembly.

Dr. Livermore is a member of ASME.